

Article

Enhanced Thermoelectric Properties of WS₂/Single-Walled Carbon Nanohorn Nanocomposites

Ji Hoon Kim ^{1,2}, Seunggun Yu ³, Sang Won Lee ⁴, Seung-Yong Lee ⁵, Keun Soo Kim ⁶,
Yoong Ahm Kim ^{2,*} and Cheol-Min Yang ^{1,*}

¹ Institute of Advanced Composite Materials, Korea Institute of Science and Technology (KIST), Wanju-gun, Jellabuk-do 55324, Korea; t16729@kist.re.kr

² Department of Polymer Engineering, Graduate School, Chonnam National University, Gwangju 61186, Korea

³ Insulation Materials Research Center, Korea Electrotechnology Research Institute (KERI), Changwon 51543, Korea; viola@keri.re.kr

⁴ Research Center for Carbon Convergence Materials, Korea Institute of Carbon Convergence Technology, Jeonju, Jeollabuk-do 54853, Korea; swonlee00@kctech.re.kr

⁵ Magok R&D Campus, LG Innotek, Seoul 07796, Korea; seungyong@lginnotek.com

⁶ Department of Physics and Graphene Research Institute-Texas Photonics Center International Research Center (GRI-TPC IRC), Sejong University, 209 Neungdong-ro, Gwangin-gu, Seoul 05006, Korea; kskim2676@sejong.ac.kr

* Correspondence: yak@chonnam.ac.kr (Y.A.K.); cmyang1119@kist.re.kr (C.-M.Y.)

Received: 23 January 2020; Accepted: 20 February 2020; Published: 24 February 2020



Abstract: Recently, two-dimensional tungsten disulfide (WS₂) has attracted attention as a next generation thermoelectric material due to a favorable Seebeck coefficient. However, its thermoelectric efficiency still needs to be improved due to the intrinsically low electrical conductivity of WS₂. In the present study, thermoelectric properties of WS₂ hybridized with highly conductive single-walled carbon nanohorns (SWCNHs) were investigated. The WS₂/SWCNH nanocomposites were fabricated by annealing the mixture of WS₂ and SWCNHs using a high-frequency induction heated sintering (HFIHS) system. By adding SWCNHs to WS₂, the nanocomposites exhibited increased electrical conductivity and a slightly decreased Seebeck coefficient with the content of SWCNHs. Hence, the maximum power factor of 128.41 μW/mK² was achieved for WS₂/SWCNHs with 0.1 wt.% SWCNHs at 780 K, resulting in a significantly improved thermoelectric figure of merit (*zT*) value of 0.027 compared to that of pristine WS₂ with *zT* 0.017.

Keywords: tungsten disulfide; single-walled carbon nanohorns; thermoelectric materials; high frequency induction heated sintering system

1. Introduction

As resources are finite and technologies advance, it is necessary to address issues impacting the global environment and energy to protect environmental degradation and achieve renewable energy [1–3]. Thermoelectric materials, which directly convert thermal energy into electrical energy, have been intensively studied. Therefore, waste heat can be recycled into useful electrical power. The conversion efficiency of thermoelectric energy is represented by a dimensionless value referred to as the figure of merit (*zT*) as per the following equation [4]:

$$zT = (\sigma S^2 \kappa^{-1}) T \quad (1)$$

where σ is the electrical conductivity; S is Seebeck coefficient; κ is thermal conductivity; and T is absolute temperature. To date, several studies have focused on designing thermoelectric materials based on

heavy elements such as Bi, Se, Te, Sb, Pb, Si, and Ge, which are usually toxic, scarce, and expensive, thereby limiting the practical applications of these materials [5–7]. Therefore, it is necessary to develop novel thermoelectric materials containing non-toxic earth-abundant elements and achieve superior performance and high thermoelectric efficiency in a wide temperature range.

Tungsten disulfide (WS_2), which is a two-dimensional layered transition metal dichalcogenide, has attracted attention as a promising thermoelectric material not only due to its environmental stability and earth-abundant elemental composition, but also low thermal conductivity (1.2–2.3 W/mK) and high Seebeck coefficient (380–1000 μ V/K) [8–10]. Despite the advantageous properties of WS_2 , its use as a thermoelectric material has been limited by a relatively low power factor and low zT value due to its intrinsically low electrical conductivity [11,12]. Therefore, the design of hybrid materials of WS_2 with highly conductive carbonaceous materials such as carbon nanotubes (CNTs) and graphene has been investigated to improve its electrical conductivity. However, incorporating carbonaceous materials led to significantly reduced Seebeck coefficients as well as poor dispersion by their agglomeration, even though the electrical conductivity was increased [12].

Recently, single-walled carbon nanohorns (SWCNHs) composed of spherical clusters of tubular graphite have been used as a substituent for conventional carbonaceous materials due to their excellent dispersion performance in various mediums, thus enabling easy composite processing [13,14]. The practical use of these SWCNHs is also advantageous because of their favorable electrical characteristics viz. low resistance value (4.3 Ω cm) as well as simple fabrication process by catalyst-free CO_2 laser ablation of a pure graphite target [15–17].

In this study, WS_2 /SWCNH nanocomposites were fabricated by annealing using a high-frequency induction heated sintering (HFIHS) system, which efficiently controls the grain size, resulting in reduced thermal conductivity and also reduces the sintering time to within a few minutes [18,19]. The morphological and structural properties of the sintered WS_2 and WS_2 /SWCNH nanocomposites were characterized. Moreover, the thermoelectric characteristics of the sintered WS_2 and WS_2 /SWCNH nanocomposites were investigated by measuring their electrical and thermal transport properties as well as carrier characteristics.

2. Materials and Methods

2.1. Preparation of Tungsten Disulfide (WS_2)/Single-Walled Carbon Nanohorn (SWCNH) Nanocomposites via High-Frequency Induction Heated Sintering (HFIHS)

Figure 1 shows a schematic illustration of the preparation process of the WS_2 /SWCNH nanocomposite through a HFIHS. WS_2 (Alfa Aesar, 99.8% metal basis) and SWCNH (Sigma Aldrich, St. Louis, MO, USA) powders with a given ratio were dispersed in ethanol under sonication at 560 W for 10 min, and then mixed together. The mixed dispersion of WS_2 and SWCNH powders was vacuum-filtrated using a polytetrafluoroethylene (PTFE) membrane filter with a pore size of 0.2 μ m (Millipore, San Francisco, CA, USA), and the sediments on the filter were dried under vacuum ($\sim 10^{-2}$ torr) for 24 h at 300 K. The dried powders of the WS_2 /SWCNH mixture were introduced into a graphite die with a diameter of 30 mm and compressed under a pressure of 10 MPa for 30 min, followed by sintering under a pressure of 50 MPa at 1450 $^{\circ}$ C and pulsed-current 2800 A for 5 min using the HFIHS system (Vacuum Science Laboratory) (Figure S1, see Supplementary Materials). For comparison, a pristine WS_2 composite was fabricated using the same methodology. As-sintered composites were cut and polished into the desired shapes for measuring thermal conductivity ($\Phi 12.7 \times 2$ mm³), electrical conductivity, and Seebeck coefficient ($2 \times 3 \times 10$ mm³) as well as carrier concentration and mobility ($10 \times 10 \times 1$ mm³). The composite specimens were denoted as WS_2 , WS_2 /SWCNH(0.1), WS_2 /SWCNH(0.5), and WS_2 /SWCNH(1.0) corresponding to 0, 0.1, 0.5, and 1.0 wt.% content of SWCNH, respectively.

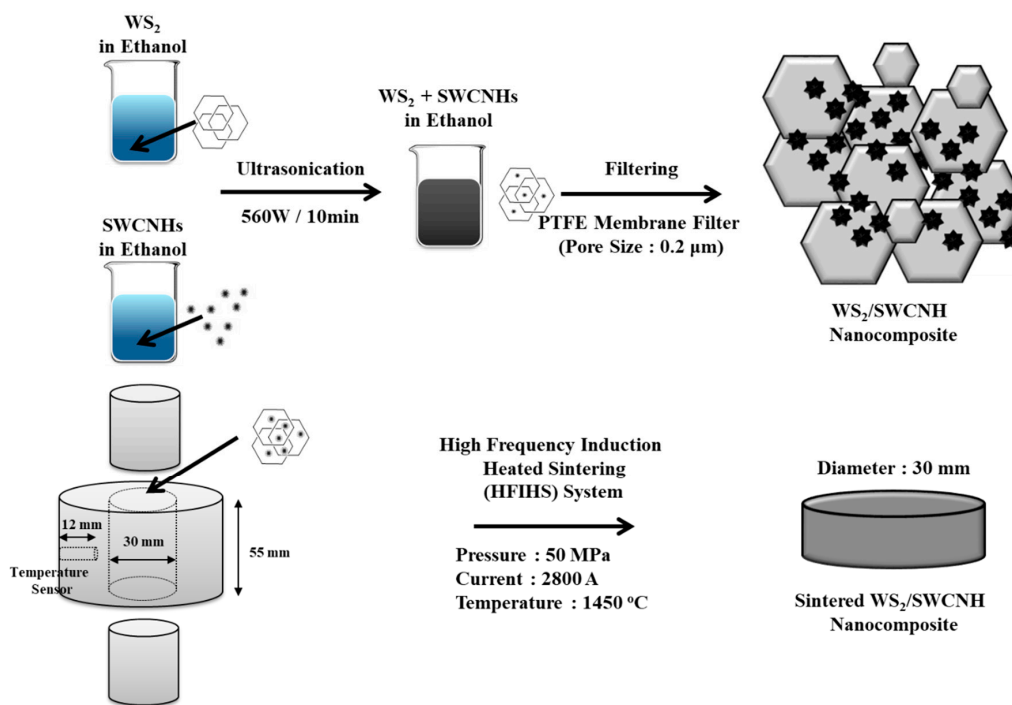


Figure 1. Schematic illustration of the preparation process of the tungsten disulfide (WS_2)/single-walled carbon nanohorn (SWCNH) nanocomposites.

2.2. Characterizations

The morphologies of the WS_2 and SWCNH powders and their composites were analyzed using field emission scanning electron microscopy (FE-SEM, Nova NanoSEM 450, FEI, Hillsboro, Oregon, USA), energy-dispersive x-ray spectroscopy (EDX, FEI, Hillsboro, Oregon, USA), and high-resolution transmission electron microscopy (HR-TEM, Tecnai G2 F20, FEI, Hillsboro, Oregon, USA). The surface chemical states of the specimens were analyzed using Raman spectroscopy with an excitation laser wavelength of 514 nm (in Via Reflex Raman microscope, Renishaw, Wotton-under-Edge, Gloucestershire, UK) and x-ray diffraction (XRD) patterns (one dimensional x-ray diffractometer, Rigaku SmartLab, Akishima-shi, Tokyo, Japan) using $CuK\alpha$ radiation (wavelength 0.154 nm). The electrical conductivity and Seebeck coefficient of the sintered composites in the in-plane direction were measured in a temperature range from 300 to 780 K in a He atmosphere using a thermoelectric measurement machine (ZEM-3 M10, ULVAC-RIKO, Chigasaki, Kanagawa, Japan). The carrier concentration and mobility were measured through the Van der Pauw method under a magnetic field of 0.56 T using a Hall effect measurement system (HMS-5000, ECOPIA, Anyang, Korea). Thermal diffusivity was measured using a laser flash method (LFA447, Netzsch, Selb, Germany) based on a Xenon flash lamp source from 300 to 780 K. The specific heat was measured using differential scanning calorimetry (DSC, Q20, TA Instruments, New Castle, Delaware, USA). The density was measured by Archimedes' method. Finally, the thermal conductivity (k) in the in-plane direction was calculated from the equation $k = T_d \times a \times \rho$, where T_d , a , and ρ are the specific heat (J/gK), thermal diffusivity (mm^2/s), and density (g/cm^3), respectively.

3. Results and Discussion

The morphologies of the SWCNHs, WS_2 , and WS_2 /SWCNH hybrids were analyzed using electron microscopy as shown in Figure 2. The FE-SEM and HR-TEM results shown in Figure 2a,b clearly exhibit the dahlia-like morphology of the SWCNHs with a diameter of approximately 90 nm. Additionally, the FE-SEM results in Figure 2c exhibit the two-dimensional hexagonal crystals of WS_2 flakes with a diameter and thickness of approximately 3.4 μm and 200 nm, respectively. After hybridization,

the SWCNHs were distributed on the surface of the WS₂ flakes with the content of SWCNHs, as shown in Figure 2d–f.

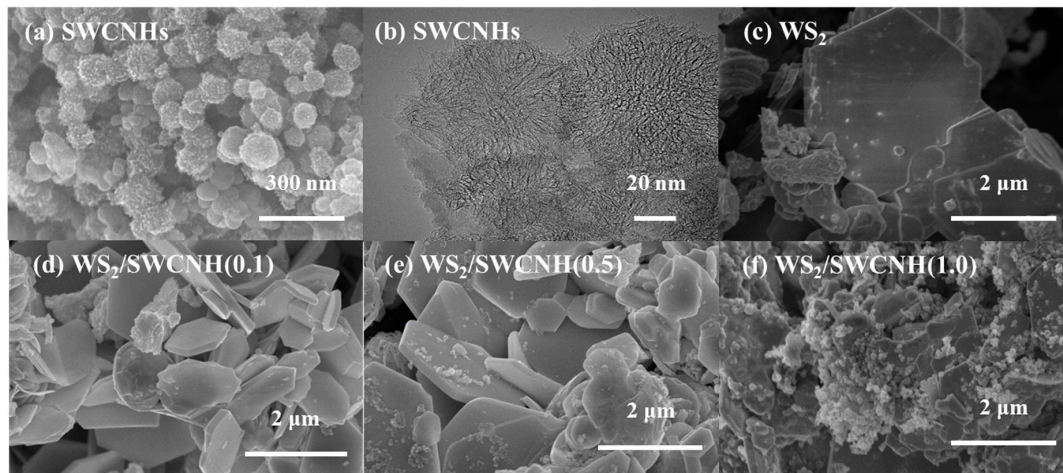


Figure 2. (a) Field emission scanning electron microscopy (FE-SEM) and (b) high-resolution transmission electron microscopy (HR-TEM) images of SWCNHs; FE-SEM image of (c) WS₂, (d) WS₂/SWCNH(0.1), (e) WS₂/SWCNH(0.5), and (f) WS₂/SWCNH(1.0).

Figure 3 shows the FE-SEM images of the as-sintered WS₂ and WS₂/SWCNH nanocomposites in the surface and cross-sectional views, respectively. The pristine bulk WS₂ exhibited the typical morphology of sintered WS₂ grains, as shown in Figure 3a (the grain sizes observed from the surface and cross-sectional views were distributed in the range of 0.5–5 and 0.5–2 μm, respectively). Introducing SWCNHs clearly reduced the grain size of WS₂ with the content of SWCNHs (the grain sizes observed from the surface and cross-sectional views were distributed in the range of 0.5–2 and 0.5–1 μm, respectively), in which the elemental fraction of C atoms from the SWCNHs increased from 13.20 to 22.84 at%, which is indicative of the successful incorporation of SWCNHs, as shown in Figure 3b–d (Figure S2). It is noteworthy that the use of SWCNHs as filler allowed for the uniform dispersion of graphitic tubules within the WS₂ matrix due to their advantageous dispersibility by morphological characteristics (Figure 4).

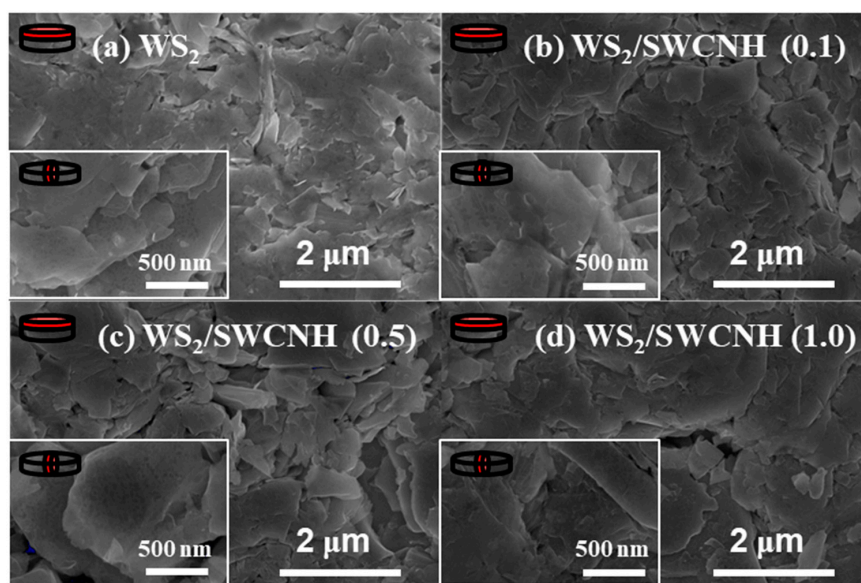


Figure 3. FE-SEM images of as-sintered (a) WS₂, (b) WS₂/SWCNH(0.1), (c) WS₂/SWCNH(0.5), and (d) WS₂/SWCNH(1.0).

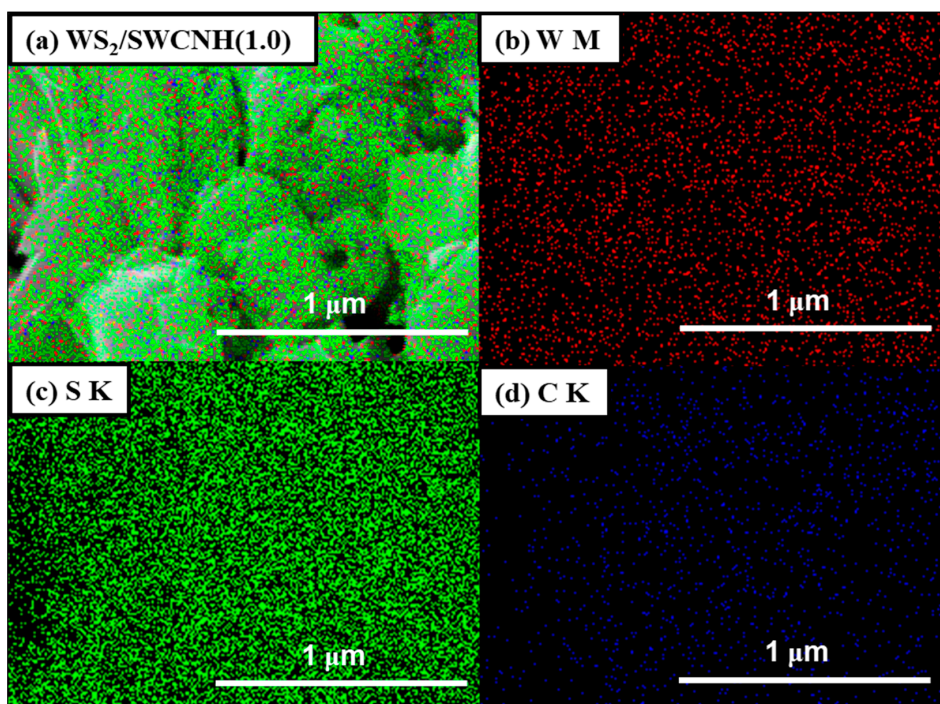


Figure 4. FE-SEM-EDX mapping of the sintered $WS_2/SWCNH(1.0)$ nanocomposite: (a) $WS_2/SWCNH(1.0)$, (b) W M, (c) S K, and (d) C K.

Figure 5 shows the Raman spectra of the sintered WS_2 and $WS_2/SWCNH$ nanocomposites. The E_{2g}^1 and A_{1g} peaks at approximately 351.25 and 420.86 cm^{-1} are attributed to the in-plane and out-of-plane vibrational modes of S atoms in the WS_2 crystal, respectively, as shown in Figure 5a [20]. Additionally, peaks were observed at approximately 1335 and 1580 cm^{-1} for the $WS_2/SWCNH$ nanocomposites, which are attributed to the defect-induced structural disorder and sp^2 hybridized bonding of carbon atoms, respectively. Based on these two distinctive peaks, the intensity ratio (R , (I_D/I_G)) can be obtained to estimate the number of sp^2 carbon clusters. The R values of the nanocomposites gradually increased from 1.23 to 1.44 with the content of SWCNHs, which was greater compared to that of the pristine SWCNH powder ($R = 1.04$) (Figure S3). This can be ascribed to the number of defects that slightly developed in SWCNHs during the high-temperature sintering process.

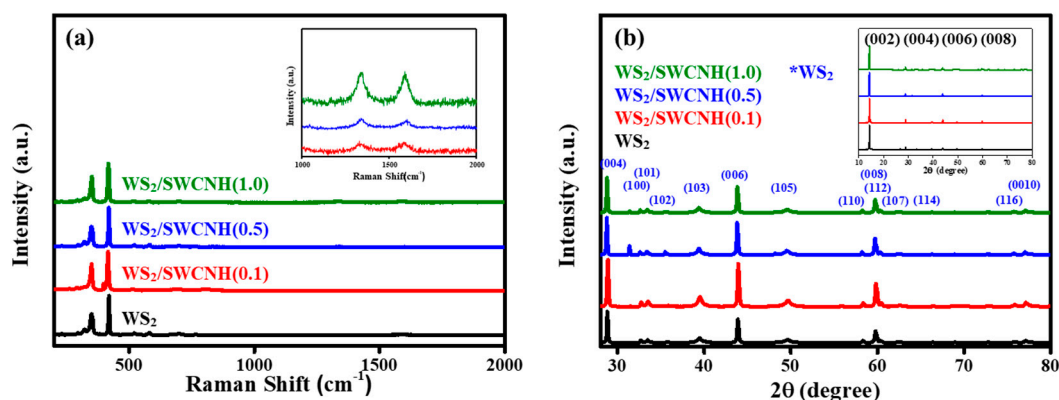


Figure 5. (a) Raman spectra and (b) x-ray diffraction (XRD) patterns of the as-sintered WS_2 and $WS_2/SWCNH$ nanocomposites. Insets show the respective magnified graphs.

The crystal characteristics of the sintered WS_2 and $WS_2/SWCNH$ nanocomposites were confirmed by XRD patterns, as shown in Figure 5b. The pristine WS_2 exhibited multiple diffraction peaks by the

phase matching for different principal planes (JCPDS #08-0237). It was also observed that the intensive peak of the (002) plane occurred at 14.28 degrees, followed by (004), (006), and (008) planes at 28.81, 43.92, and 59.73 degrees, respectively, which is attributed to the layered nature of the WS₂ flakes [21,22]. After sintering, the whole samples maintained the characteristic peaks from WS₂, indicative of the independent grain growth of WS₂ regardless of the existence of SWCNHs. In addition, the peaks from the tungsten carbide (WC) phase were not observed, despite the possible formation of WC with SWCNHs under high-temperature annealing. This can be attributed to the lower concentration of SWCNHs in the composite.

The majority carrier behavior of the sintered WS₂ and WS₂/SWCNH nanocomposites were analyzed by measuring the carrier concentration (n) and mobility (μ) at 300 K based on the Van der Pauw method, as shown in Figure 6a. The pristine WS₂ exhibited approximately $5.82 \times 10^{15} \text{ cm}^{-3}$ of carrier concentration. By adding SWCNHs, the value was gradually increased with the content of SWCNHs to $4.51 \times 10^{17} \text{ cm}^{-3}$. Meanwhile, the maximum carrier mobility of $27.76 \text{ cm}^2/\text{Vs}$ was achieved in the WS₂/SWCNH(0.5), followed by a decrease to $8.95 \text{ cm}^2/\text{Vs}$ in the WS₂/SWCNH(1.0). It is assumed that the excess amount of SWCNHs causes large carrier scattering at the enlarged interfaces between SWCNHs and WS₂ [23].

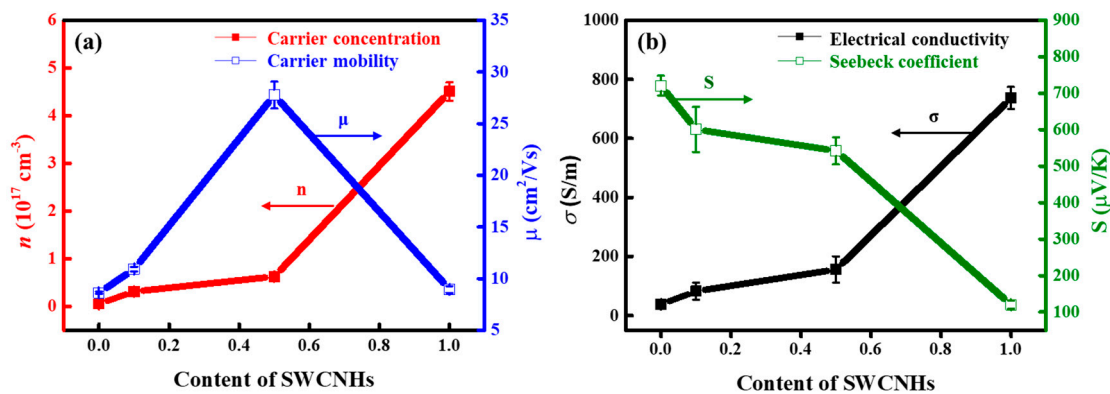


Figure 6. (a) Carrier concentration and carrier mobility plots. (b) Electrical conductivity and Seebeck coefficient of the WS₂/SWCNH nanocomposites with the content of SWCNHs.

The thermoelectric properties of the sintered WS₂ and WS₂/SWCNH nanocomposites were evaluated by considering the carrier behavior, as shown in Figure 6b. The electrical conductivity (σ) is proportional to the carrier concentration and mobility as per the following equation (e is charge of electron: $1.6 \times 10^{19} \text{ C}$):

$$\sigma = ne\mu \quad (2)$$

The pristine WS₂ exhibited an electrical conductivity of 38.18 S/m, and the value increased to 737.19 S/m in the WS₂/SWCNH(1.0), which is approximately 19 times greater than that of the pristine WS₂ sample because SWCNHs have an intrinsically higher electrical conductivity [24]. The electrical conductivity values were also identical to the trend of carrier concentration, because the difference in carrier concentration was significantly greater than the carrier mobility change. However, the Seebeck coefficient (S) is inversely proportional to carrier concentration (n) as per the following equation [23]:

$$S = \frac{8\pi^2 k_B^2}{3eh^2} m^* T \left(\frac{\pi}{3n}\right)^{2/3} \quad (3)$$

where k_B is the Boltzmann constant; h is the Planck constant; m^* is the effective mass of charge carrier; and T is the absolute temperature. In our measurement environment, the generated voltage with temperature difference (ΔT) indicates reliability with linear slope (Figure S4a). The pristine WS₂

exhibited a Seebeck coefficient of 700.78 $\mu\text{V}/\text{K}$. By adding SWCNHs, the values of the nanocomposites gradually decreased with the content of SWCNHs due to the increase in carrier concentration.

The temperature dependent thermoelectric properties of the sintered WS_2 and WS_2/SWCNH nanocomposites were further investigated between 300 and 780 K, as shown in Figure 7. The electrical conductivity values of the whole samples increased with temperature, indicating conventional semiconductor like behavior, as shown in Figure 7a [25]. The pristine WS_2 exhibited an electrical conductivity of 125.51 S/m at 780 K. By adding SWCNHs, the electrical conductivity of the nanocomposites is increased to 1181.37 S/m for $\text{WS}_2/\text{SWCNH}(1.0)$, which was similar to the behavior at room temperature.

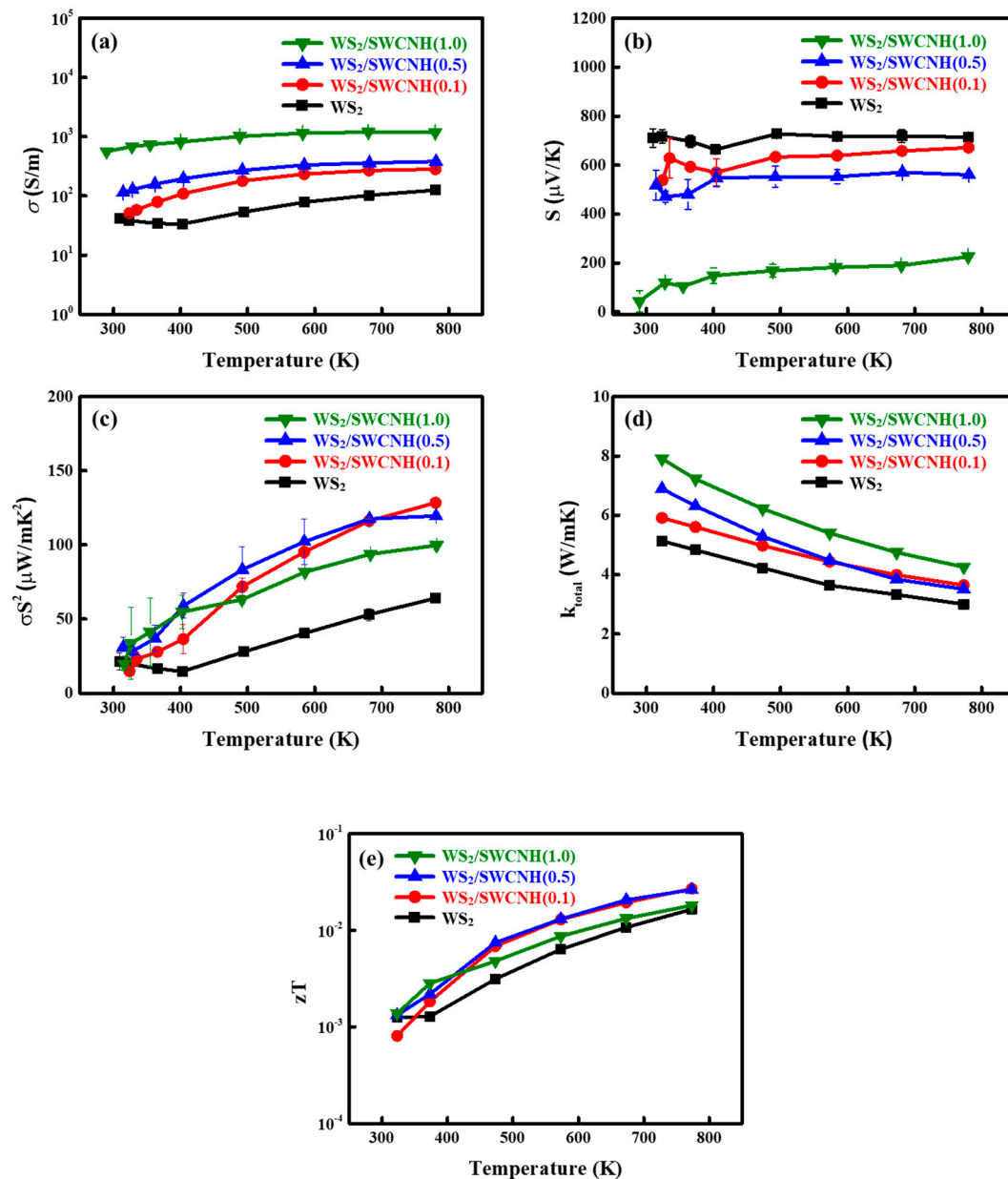


Figure 7. (a) Electrical conductivity, (b) Seebeck coefficient, (c) power factor, (d) thermal conductivity, and (e) dimensionless figure of merits of the WS_2/SWCNH nanocomposites with temperature.

The pristine WS_2 exhibited a Seebeck coefficient of 710.53 $\mu\text{V}/\text{K}$ at 300 K and the value increased by 714.32 $\mu\text{V}/\text{K}$ at 780 K, as shown in Figure 7b. Meanwhile, the Seebeck coefficient values were gradually decreased by adding the SWCNHs in the complete temperature range, and reached a

minimum for the WS₂/SWCNH(1.0). As per Equation (3), by considering the dependence on increased carrier concentration, the Seebeck coefficient decreased with the content of SWCNHs. Additionally, the whole samples of WS₂/SWCNH nanocomposites showed less temperature dependency on the Seebeck coefficient with a slightly increased value.

The power factor (*PF*) values of the WS₂ and WS₂/SWCNH nanocomposites were calculated from the equation $PF = \sigma S^2$, as shown in Figure 7c. The power factor values of the samples increased with temperature, which depends on the electrical conductivity behavior. The highest power factor value was obtained for WS₂/SWCNH(0.1) due to the increased electrical conductivity and slightly reduced Seebeck coefficient. The WS₂/SWCNH(0.1) exhibited a power factor value of 14.93 $\mu\text{W}/\text{mK}^2$ at 300 K, and the value was increased to 128.41 $\mu\text{W}/\text{mK}^2$ at 780 K.

The thermal conductivity, which is an important thermoelectric property, was measured for the WS₂ and WS₂/SWCNH nanocomposites, as shown in Figure 7d. The thermal conductivity values decreased with temperature, thus indicative of the dominant Umklapp phonon–phonon scattering [26]. The pristine WS₂ exhibited a thermal conductivity of 3.0 W/mK, while the WS₂/SWCNH(1.0) exhibited a slightly higher value of 4.25 W/mK at 780 K. The total thermal conductivity (κ_{total}) is calculated as the sum of electronic and lattice vibrational contributions as per the following equation [23]:

$$\kappa_{total} = \kappa_e + \kappa_l = L\sigma T + \kappa_l \quad (4)$$

where κ_e is the electronic thermal conductivity, and κ_l is the phononic thermal conductivity by lattice vibration. For the WS₂ and WS₂/SWCNH nanocomposites, the phonons traveling by lattice vibration were responsible for the total thermal conductivity rather than the electronic contribution because electronic thermal conductivity is negligible (Figure S4c–d). The total thermal conductivity increased with the content of SWCNHs, which is likely due to the percolation of segregated SWCNHs with individually high thermal conductivity arising from their graphitic structure [27].

The thermoelectric figure of merit (*zT*) of the WS₂ and WS₂/SWCNH nanocomposites were investigated using Equation (1), as shown in Figure 7e. In total, the *zT* values of the whole samples increased with temperature due to the increased electrical conductivities without a reduction in Seebeck coefficient, which dramatically reduced the thermal conductivities. The *zT* value of WS₂/SWCNH(0.1) yielded a maximum of 0.027 at 780 K, which was 1.63 times greater than that of the pristine WS₂. Thus, the use of SWCNHs to control the carrier concentration is beneficial for improving electrical properties, giving rise to achieving high *zT* values for next generation thermoelectric materials.

4. Conclusions

Thermoelectric WS₂/SWCNH nanocomposites were fabricated by physically mixing two-dimensional WS₂ flakes and dahlia-like SWCNHs, followed by annealing using a HFIHS system. In the sintered WS₂/SWCNH nanocomposites, the SWCNHs were homogeneously dispersed at the interfaces of the aggregated WS₂ flakes without the unnecessary formation of secondary phases. The electrical conductivity of the nanocomposites was significantly improved with the content of SWCNHs, while the Seebeck coefficient was slightly decreased depending on the carrier concentration and mobility. Combining the electrical conductivity and Seebeck coefficient, the power factor of the composite achieved a value of 128.41 $\mu\text{W}/\text{mK}^2$ at 780 K for the WS₂/SWCNH(0.1). Furthermore, the improved power factor allowed for a maximum *zT* value of 0.027 at 780 K for WS₂/SWCNH(0.1), which was 1.63 times greater than that of pristine WS₂, and the thermal conductivity increased with the percolation of SWCNHs. Therefore, designing WS₂ hybridized with SWCNHs suggests a new strategy to improve their thermoelectric performance by controlling electrical properties. We expect that our approach for producing WS₂/SWCNH nanocomposites with enhanced thermoelectric properties can contribute to the development of thermoelectric devices such as radioisotope thermoelectric generators and wearable thermoelectric devices.

Supplementary Materials: The following are available online at <http://www.mdpi.com/2073-4352/10/2/140/s1>. Figure S1: Sintering profiles and mass densities of the sintered WS₂ and WS₂/SWCNH nanocomposites. Figure S2: FE-SEM-EDX of the sintered WS₂ and WS₂/SWCNH nanocomposites. Figure S3: Raman spectrum of the SWCNH powder. Table S1: Raman factors of the SWCNH powder. Table S2: Raman factors of the sintered WS₂ and WS₂/SWCNH nanocomposites. Figure S4: Thermoelectric characteristics of the sintered WS₂ and WS₂/SWCNH nanocomposites.

Author Contributions: C.-M.Y., S.W.L., and Y.A.K. were responsible for initiating and designing the research. J.H.K., S.-Y.L., and K.S.K. performed the experiments and analyzed the data. J.H.K., S.Y., and C.-M.Y. wrote the paper. All authors have read and agreed to the published version of the manuscript.

Funding: This project was supported by a grant from the Korea Institute of Science and Technology (KIST) Institutional Program and Nano-Material Technology Development Program through the National Research Foundation of Korea (NRF) funded by the Ministry of Science (2016M3A7B4027695). S.W. Lee acknowledges the financial support from the Regional Leading Research Center Program through the National Research Foundation of Korea (NRF) funded by the Ministry of Science and ICT of the Republic of Korea (2019R1A5A8080326). K.S. Kim acknowledges the financial support from the National Research Foundation of Korea (NRF) grant funded by the Korean government (MSIT) (2019R1A2C1009963).

Conflicts of Interest: The authors declare no conflicts of interest.

References

1. Bell, L.E. Cooling, Heating, generating power, and recovering waste heat with thermoelectric systems. *Science* **2008**, *321*, 1457–1461. [[CrossRef](#)] [[PubMed](#)]
2. Omer, A.M. Energy, environment and sustainable development. *Renew. Sustain. Energy Rev.* **2008**, *12*, 2265–2300. [[CrossRef](#)]
3. Glenk, G.; Stefan, R. Economics of converting renewable power to hydrogen. *Nat. Energy* **2019**, *4*, 216–222. [[CrossRef](#)]
4. Harman, T.C.; Taylor, P.J.; Walsh, M.P.; LaForge, B.E. Quantum dot superlattice thermoelectric materials and devices. *Science* **2002**, *297*, 2229–2232. [[CrossRef](#)]
5. Zheng, G.; Su, X.L.; Li, X.R.; Liang, T.; Xie, H.Y.; She, X.Y.; Yan, Y.G.; Uher, C.; Kanatzidis, M.G.; Tang, X.F. Toward high-thermoelectric-performance large-size nanostructured BiSbTe alloys via optimization of sintering-temperature distribution. *Adv. Energy Mater.* **2016**, *6*, 1600595. [[CrossRef](#)]
6. Pei, Y.Z.; LaLonde, A.; Iwanaga, S.; Snyder, G.J. High thermoelectric figure of merit in heavy hole dominated PbTe. *Energy Environ. Sci.* **2011**, *4*, 2085–2089. [[CrossRef](#)]
7. Heremans, J.P.; Jovovic, V.; Toberer, E.S.; Saramat, A.; Kurosaki, K.; Charoenphakdee, A.; Yamanaka, S.; Snyder, G.J. Enhancement of thermoelectric efficiency in PbTe by distortion of the electronic density of states. *Science* **2008**, *321*, 554–557. [[CrossRef](#)]
8. Coleman, J.N.; Lotya, M.; O'Neill, A.; Bergin, S.D.; King, P.J.; Khan, U.; Young, K.; Gaucher, A.; De, S.; Smith, R.J.; et al. Two-dimensional nanosheets produced by liquid exfoliation of layered materials. *Science* **2011**, *331*, 568–571. [[CrossRef](#)]
9. Kim, J.-Y.; Choi, S.-M.; Seo, W.-S.; Cho, W.-S. Thermal and electronic properties of exfoliated metal chalcogenides. *Bull. Korean Chem. Soc.* **2010**, *31*, 3225–3227. [[CrossRef](#)]
10. Solanki, G.K.; Gujarathi, D.N.; Deshpande, M.P.; Lakshminarayana, D.; Agarwal, M.K. Transport property measurements in tungsten sulphoselenide single crystals grown by a CVT technique. *Cryst. Res. Technol.* **2008**, *43*, 179–185. [[CrossRef](#)]
11. Huang, Z.; Wu, T.; Kong, S.; Meng, Q.-L.; Zhuang, W.; Jiang, P.; Bao, X. Enhancement of anisotropic thermoelectric performance of tungsten disulfide by titanium doping. *J. Mater. Chem. A* **2016**, *4*, 10159–10165. [[CrossRef](#)]
12. Georgiou, T.; Jalil, R.; Belle, B.D.; Britnell, L.; Gorbachev, R.V.; Morozov, S.V.; Kim, Y.J.; Gholinia, A.; Haigh, S.J.; Makarovskiy, O.; et al. Vertical field-effect transistor based on graphene-WS₂ heterostructures for flexible and transparent electronics. *Nat. Nanotechnol.* **2013**, *8*, 100–103. [[CrossRef](#)]
13. Iijima, S.; Yudasaka, M.; Yamada, R.; Bandow, S.; Suenaga, K.; Kokai, F.; Takahashi, K. Nano-aggregates of single-walled graphitic carbon nano-horns. *Chem. Phys. Lett.* **1999**, *309*, 165–170. [[CrossRef](#)]
14. Hwang, H.; Kim, C.H.; Wee, J.-H.; Han, J.H.; Yang, C.-M. High-density graphene/single-walled carbon nanohorn composite supercapacitor electrode with high volumetric capacitance. *Appl. Surf. Sci.* **2019**, *489*, 708–716. [[CrossRef](#)]

15. Jung, H.J.; Kim, Y.-J.; Han, J.H.; Yudasaka, M.; Iijima, S.; Kanoh, H.; Kim, Y.A.; Kaneko, K.; Yang, C.-M. Thermal-treatment-induced enhancement in effective surface area of single-walled carbon nanohorns for supercapacitor application. *J. Phys. Chem. C* **2013**, *117*, 25877–25883. [[CrossRef](#)]
16. Yang, C.-M.; Kim, Y.-J.; Endo, M.; Kanoh, H.; Yudasaka, M.; Iijima, S.; Kaneko, K. Nanowindow-regulated specific capacitance of supercapacitor electrodes of single-wall carbon nanohorns. *J. Am. Chem. Soc.* **2007**, *129*, 20–21. [[CrossRef](#)]
17. Yang, C.-M.; Noguchi, H.; Murata, K.; Yudasaka, M.; Hashimoto, A.; Iijima, S.; Kaneko, K. Highly ultramicroporous single-walled carbon nanohorn assemblies. *Adv. Mater.* **2005**, *17*, 866–870. [[CrossRef](#)]
18. Khasimsaheb, B.; Singh, N.K.; Bathula, S.; Gahtori, B.; Haranath, D.; Neeleshwar, S. The effect of carbon nanotubes (CNT) on thermoelectric properties of lead telluride (PbTe) nanocubes. *Curr. Appl. Phys.* **2017**, *17*, 306–313. [[CrossRef](#)]
19. Ren, F.; Wang, H.; Menchhofer, P.A.; Kiggans, J.O. Thermoelectric and mechanical properties of multi-walled carbon nanotube doped $\text{Bi}_{0.4}\text{Sb}_{1.6}\text{Te}_3$ thermoelectric material. *Appl. Phys. Lett.* **2013**, *103*, 221907. [[CrossRef](#)]
20. Zhou, H.; Yu, F.; Sun, J.; He, R.; Wang, Y.; Guo, C.F.; Wang, F.; Lan, Y.; Ren, Z.; Chen, S. Highly active and durable self-standing WS_2 /graphene hybrid catalysts for hydrogen evolution reaction. *J. Mater. Chem. A* **2016**, *4*, 9472–9476. [[CrossRef](#)]
21. Lim, Y.V.; Wang, Y.; Kong, D.; Guo, L.; Wong, J.I.; Ang, L.K.; Yang, H.Y. Cubic-shaped WS_2 nanopetals on a Prussian blue derived nitrogen-doped carbon nanoporous framework for high performance sodium-ion batteries. *J. Mater. Chem. A* **2017**, *5*, 10406–10415. [[CrossRef](#)]
22. Sharma, S.; Bhagat, S.; Singh, J.; Singh, R.C.; Sharma, S. Excitation-dependent photoluminescence from WS_2 nanostructures synthesized via top-down approach. *J. Mater. Sci.* **2017**, *52*, 11326–11336. [[CrossRef](#)]
23. Biswas, K.; He, J.; Zhang, Q.; Wang, G.; Uher, C.; Dravid, V.P.; Kanatzidis, M.G. Strained endotaxial nanostructures with high thermoelectric figure of merit. *Nat. Chem.* **2011**, *3*, 160–166. [[CrossRef](#)]
24. Bera, R.; Karan, S.K.; Das, A.K.; Paria, S.; Khatua, B.B. Single wall carbon nanohorn (SWCNH)/graphene nanoplate/poly(methyl methacrylate) nanocomposites: a promising material for electromagnetic interference shielding applications. *RSC Adv.* **2015**, *5*, 70482–70493. [[CrossRef](#)]
25. Zevalkink, A.; Toberer, E.S.; Zeier, W.G.; Flage-Larsen, E.; Snyder, G.J. Ca_3AlSb_3 : an inexpensive, non-toxic thermoelectric material for waste heat recovery. *Energy Environ. Sci.* **2011**, *4*, 510–518. [[CrossRef](#)]
26. Freedman, J.P.; Leach, J.H.; Preble, E.A.; Sitar, Z.; Davis, R.F.; Malen, J.A. Universal phonon mean free path spectra in crystalline semiconductors at high temperature. *Sci. Rep.* **2013**, *3*, 2963. [[CrossRef](#)]
27. Selvam, C.; Harish, S.; Lal, D.M. Effective thermal conductivity and rheological characteristics of ethylene glycol-based nanofluids with single-walled carbon nanohorn inclusions. *Fullerenes Nanotubes Carbon Nanostruct.* **2017**, *25*, 86–93. [[CrossRef](#)]

